Computational Investigation of Inclusion Removal in the Steel-Refining Ladle Process

Xipeng Guo [1], Joel Godinez [1], Nicholas J. Walla [1], Armin K. Silaen [1], Helmut Oltmann [2], Vivek Thapliyal [2], Abhishek Bhansali [2], Eugene Pretorius [2] and Chenn Q. Zhou [1,*]

1   Center for Innovation through Visualization and Simulation, Purdue University Northwest, 2200 169th Street, Hammond, IN 46323, USA; guo468@pnw.edu (X.G.); jpgodine@pnw.edu (J.G.); njwalla@pnw.edu (N.J.W.); asilaen@pnw.edu (A.K.S.)
2   Nucor Steel, 3401 Process Dr NW, Decatur, AL 35601, USA; Helmut.Oltmann@nucor.com (H.O.); vivek.thapliyal@nucor.com (V.T.); abhishek.bhansali@nucor.com (A.B.); eugene.pretorius@nucor.com (E.P.)
*   Correspondence: czhou@pnw.edu; Tel.: +1-219-989-2665

Abstract: In a steel-refining ladle, the properties of manufactured steel can be notably degraded due to the presence of excessive inclusions. Stirring via gas injection through a porous plug is often used as part of the steel-refining process to reduce these inclusions. In this paper, 3D computational fluid dynamics (CFD) modeling is used to analyze transient multiphase flow and inclusion removal in a gas-stirred ladle. The effects of gas stirring with bubble-inclusion interaction are analyzed using the Euler–Euler approach for multiphase flow modeling, while the effects of inclusions aggregation and removal are modeled via a population balance model (PBM).

1. Introduction

In the control of steel cleanliness, non-metallic inclusion removal is largely accomplished (65–75%) through ladle operations. Non-metallic inclusions directly affect steel products' fatigue strength, impact toughness, corrosion resistance, and machinability factors such as cutting force, chip/crack formation, power consumption, and tool wear. Non-metallic inclusions can also lead to excessive casting repairs and rejected castings. Cumulatively, these factors negatively impact U.S. energy use and efficiency, infrastructure, economic competitiveness, and national security, because high-quality steel products are keystone parts of fundamental transportation, construction, communications, and defense systems.

In the past few decades, several researchers have investigated inclusion behavior and flow characteristics in a gas-stirred refining ladle. In 1975, Szekely et al. [1] first modeled and studied the flow characteristic in a ladle based on a simplified water model. Gas was injected from the bottom of the ladle with an assumed constant bubble size, and all other boundary conditions were sourced from the physical experiment. By using Spalding's k-ω model, the Navier-Stokes equations were solved to predict velocity and turbulence in a water model. In 1978, DebRoy et al. [2] improved Szekely et al.'s model by revising the bubble model from dispersed bubbles constrained in a single plume with a diameter related to volume fraction to injection based on gas flow rate. Johansen et al. [3] performed experiments by using a bottom injection water model, discovering key interactions between bubble-generated turbulence and flow velocity in the bubble plume region.

Peranandhantan et al. [4] conducted experiments to study the formation and size of a slag eye in a simplified water model. Several variables such as gas flow rate, slag thickness, and liquid depth were explored in their work. The slag eye was captured and measured through visual inspection with a camera. Mazumdar et al. [5] reviewed several studies on physical models and empirical correlations of gas-stirred ladles, covering various simplified

expressions of several variables, including gas flow rate and ladle dimensions, among others. Guo et al. [6] developed a 3-D CFD ladle simulation using a Lagrangian–Eulerian model to predict gas-liquid two-phase flow in the ladle. In this work, more detailed models such as lateral drag force and lift force and so on were added to predict the plume shape. Plume spreading and mass transfer to rising bubbles and the top free surface are included. Zhang et al. [7] developed a Eulerian–Eulerian two-phase flow system for ladle, with the k-ε turbulence model used to simulate turbulence inside of the ladle. Lou et al. [8] developed a Eulerian–Eulerian numerical model to simulate gas-liquid two-phase flow in the bottom injection gas-stirred system. The effect of the turbulent dispersion force, drag force, and lift force upon the flow field were studied. A bubble-induced turbulence term was developed and included as a source term in order to more accurately predict the bubble plume shape.

For the inclusion removal process, Lou et al. [9] conducted a review of inclusion behavior mechanisms, including inclusion aggregation and removal. In the past several decades, beginning in the 1970s, researchers have applied numerical methods to calculate and analyze inclusion behavior. In 1975, Szekely et al. [1] utilized a 2-D model to study inclusion aggregation by inclusion turbulence collision. In 1983, Shirabe et al. [10] also developed a 2-D model to predict inclusion aggregation by inclusion turbulence collision. However, consideration of all the mechanisms, including inclusion aggregation and inclusion removal was not made. In 2001, Mats Söder [11] discussed the four mechanisms of inclusion aggregation and all three inclusion removal mechanisms. Four different bubble removal models were compared in this thesis, and more detail was added on inclusion removal due to inclusion-bubble interaction. In this study, inclusion-bubble interactions, including turbulence random collision, turbulence shear collision, laminar shear collision, and stokes collision, were considered. In 2005, Wang et al. [12] reviewed the inclusion removal process and proposed an expression to represent inclusion removal probability. The expression is related to the probability of adhesion, collision, and detachment. In the study, the author also mentioned that detachment is nearly negligible. In 2013, Lou et al. [9] performed a more detailed study of inclusion behavior in refining ladles utilizing three inclusion aggregation mechanisms and six inclusion removal mechanisms. In 2019, Chen et al. [13] first validated simulated inclusion removal results with measured data using the inhomogeneous discrete method of the population balance model.

The intent of this work is to build upon previous studies on flow characteristics and inclusion behavior conducted by researchers at Purdue University Northwest's Center for Innovation through Visualization and Simulation (CIVS) to develop a comprehensive CFD ladle model capable of analyzing the effects of gas stirring on a steel-refining ladle, with particular attention to the methods by which inclusions are floated, grow, and are removed from the steel melt. The effects of gas stirring on flow in the ladle, including the impacts of bubble-inclusion interaction, are analyzed using the Euler–Euler approach for multiphase flow modeling. The effects of inclusion aggregation and removal are subsequently modeled via the population balance model (PBM). Through the development of an inclusion removal model and subsequent simulations of flow, inclusion floatation, and inclusion removal within a steel-refining ladle, a better understanding of the mixing and cleaning process can be obtained, and further studies using this modeling approach can be utilized to improve mixing time, enhance steel quality, and minimize potential defects in the downstream steelmaking process.

2. Methodology and CFD Models

The commercially available CFD software ANSYS Fluent 2020R1 was used in this research, with user-defined functions developed specifically for calculating the inclusion aggregation and removal. The simulation process utilized in this study consists of two stages: flow field simulation and inclusion removal simulation. The flow field is simulated using the Euler–Euler multiphase method. In this stage, only two phases are included: liquid steel and injected argon gas. After the multiphase flow simulation in this stage

reaches a quasi-steady state, the population balance model will be activated to simulate the inclusion aggregation and removal process. In this second stage, two inclusion phases, inclusion A and inclusion B, are considered. In phase inclusion A, the inclusion aggregation mechanism is activated, allowing smaller inclusions to agglomerate into larger inclusions. This is not the case for inclusion phase B. During the simulation, when inclusion is considered "attached" to a bubble, it will be transferred from inclusion phase A to inclusion phase B. Initial inclusion number density distribution is adopted from published measurements performed by Miyashita et al. [14]. Here, the initial inclusion number density is assumed as $2.621 \times 10^{12}/m^3$ [13]. The equation of initial number density distribution is shown below:

$$n\left(V_{i,j}, t = 0\right) = n(V_i, t = 0)EXP\left(-0.63 \times d_j \times 10^6\right) \tag{1}$$

where $n\left(V_{i,j}, t = 0\right)$ and $n(V_i, t = 0)$ are initial inclusion number density with specific size j and initial total inclusion number density.

The balance of mass and momentum of each phase is solved individually. In addition to the standard Navier-Stokes transport equations, population balance modeling based on the PBE is used to handle the transport of particle number density in the fluid, accounting for inclusion aggregation and removal. The turbulence field is predicted by using the standard k-ε model.

2.1. Continuity Equation

The general continuity equation based on Eulerian – Eulerian multiphase model can be expresed as:

$$\frac{\partial}{\partial t}\left(\alpha_m \rho_m \vec{u}_m\right) + \nabla \cdot \left(\alpha_m \rho_m \vec{u}_m\right) = S_m \tag{2}$$

α_m represents the phase volume fraction, ρ_m is the phase density, and $\vec{u}_m$ is the phase local velocity. For the left side, S_m is source term from phase m.

2.2. Momentum Equation

The momentum of each phase is solved individually, the general momentum equation can be expressed as:

$$\frac{\partial}{\partial t}\left(\alpha_m \rho_m \vec{u}_m\right) + \nabla \cdot \left(\alpha_m \rho_m \vec{u}_m \vec{u}_m\right) = -\alpha_m \nabla p + \nabla \cdot \bar{\bar{\tau}}_m + \alpha_m \rho_m \vec{g} + \vec{F}_{sum} \tag{3}$$

where $\bar{\bar{\tau}}_m$ represents phase m stress-strain tensor; $\vec{F}_{sum}$ is the summation of rest of forces, including virtual mass force, drag force, and turbulence dispersion force [8].

2.3. Turbulence Model

In the study, standard k-ε model is used to model the turbulence field in the ladle.

$$\frac{\partial}{\partial t}(\rho k) + \frac{\partial}{\partial x_m}(\rho k u_m) = \frac{\partial}{\partial x_n}\left[\left(\mu + \frac{\mu_t}{\sigma_k}\right)\frac{\partial k}{\partial x_n}\right] + G_k + G_b - \rho\varepsilon + S_k \tag{4}$$

$$\frac{\partial}{\partial t}(\rho\varepsilon) + \frac{\partial}{\partial x_m}(\rho\varepsilon u_i) = \frac{\partial}{\partial x_n}\left[\left(\mu + \frac{\mu_t}{\sigma_\varepsilon}\right)\frac{\partial\varepsilon}{\partial x_n}\right] + C_{1\varepsilon}\frac{\varepsilon}{k}C_{3\varepsilon}G_b - \rho C_2\frac{\varepsilon^2}{k + \sqrt{v\varepsilon}} + S_\varepsilon \tag{5}$$

where $C_{1\varepsilon}$ and C_2 are constant, and G_k and G_b are the turbulent kinetic energy generation due to velocity gradients and buoyancy. S_k and S_ε represent source terms to turbulent kinetic energy and turbulence dissipation rate. In this study, bubble-induced turbulence [8] is considered via a source term added into a user-defined function, which was hooked in the simulation.

2.4. Population Balance Model

Population Balance Modeling (PBM) is based on the Population Balance Equation (PBE). In the study, only inclusion aggregation and removal is considered. Inclusion growth and breakup will not be involved. The transport equation for number density of particles can be express as:

$$\frac{\partial n(V_j,t)}{\partial t} + \nabla \cdot \left(\overrightarrow{u_p} n(V_j)\right) = \frac{1}{2}\int_0^{V_k} A(V_k - V_j, V_j)n(V_k - V_j, t)n(V_j, t)\mathrm{d}V_j - \int_0^{V_{max}} A(V_k, V_j)n(V_i, t)\mathrm{d}V_j + S_j \tag{6}$$

where $n(V_j, t)$ is the number density of j size inclusions. A represents the aggregation rate of inclusion from size j to size k. S_j is external source term, and it can be used to calculate inclusion removal.

2.5. Inclusion Aggregation Model

There are three main mechanisms of inclusion aggregation widely studied. They are Brownian motion aggregation, turbulence collision aggregation, and stokes buoyancy collision aggregation. Brownian motion aggregation is neglected since it takes some time for particles to grow [15]. The overall inclusion aggregation rate can be calculated as follows:

$$A_{jk} = A_{jk}^T + A_{jk}^S \tag{7}$$

where A_{jk}^T, A_{jk}^S represent inclusion the aggregation rate from turbulence collision aggregation and stokes buoyancy collision aggregation. j and k represent two different sizes of colliding inclusions.

In a turbulent flow field, the smallest eddy size is called Kolmogorov microscale (K), and it can be expressed as:

$$K = \left(\frac{\vartheta^3}{\varepsilon}\right)^{\frac{1}{4}} \tag{8}$$

In general, in the turbulence field, particle aggregation can occur by viscous mechanism and inertia mechanism. A viscous mechanism occurs when the size of colliding particles is smaller than the Kolmogorov microscale, while an inertia mechanism occurs when the size of colliding particles is greater than the Kolmogorov microscale. Based on Saffman and Turner [16], the inclusion aggregation due to viscous mechanism can be express as:

$$A_{jk}^T = 1.294 E_t \left(\frac{\varepsilon}{\vartheta}\right)^{0.5} (r_j + r_k)^3 \tag{9}$$

$$E_t = 0.732 \left(\frac{5}{N_T}\right)^{0.242}, \ N_T \geq 5 \tag{10}$$

$$N_T = \frac{6\pi\mu_l(r_j + r_k)^3 \left(\frac{4\varepsilon}{15\pi\vartheta_l}\right)^{0.5}}{8\mathrm{H}_c} \tag{11}$$

where E_t is the capture efficiency of two colliding inclusions. N_T is the force coefficient. H_c is the Hamaker constant and can be assigned to 2.3×10^{-20}.

As for the inertia mechanism, the aggregation rate is expressed as: [17]

$$A_{jk}^T = 2.828 E_t(\pi)^{0.5}(r_j + r_k)^2 \left(u_j^2 + u_k^2\right)^{0.5} \tag{12}$$

where E_t is capture efficiency of two colliding inclusion. u_j is inclusion velocity with size d_j.

Another inclusion aggregation mechanism is Stokes buoyancy collision aggregation. Because of density difference, alumina inclusion can rise up. When inclusions rise up, the

flow field can influence the inclusion rising path. The inclusion aggregation rate due to Stokes buoyancy collision can be expressed as [13]:

$$A_{jk}^S = \frac{\pi}{4}(d_j + d_k)^2 \left| u_j^S - u_k^S \right| E_t^s \tag{13}$$

$$E_t^s = 0.732 \left(\frac{5}{N_T^s} \right)^{0.242} \tag{14}$$

$$N_T^s = 24 \sqrt{\frac{\pi}{15}} \frac{\mu_l}{H_c} (r_j + r_k)^3 \frac{\left| u_j^S - u_k^S \right|}{d_j + d_k} \tag{15}$$

$$u_p^S = \frac{g(\rho_l - \rho_p)d_p^2}{18\mu_l} \tag{16}$$

where E_t^s represents the capture efficiency of two colliding inclusions due to the stokes buoyancy collision aggregation, and u_p^S is the stokes velocity calculated from stokes law.

2.6. Inclusion Removal Model

There three different inclusion removal mechanisms: inclusion removal due to wall adhesion, inclusion removal due to slag absorption and inclusion removal due to bubble attachment. The overall inclusion removal rate is the summation of the rate from these mechanisms:

$$R_j = R_j^{wall} + R_j^{slag} + R_j^{bubble} \tag{17}$$

The first part of inclusion removal will be wall adhesion. Based on Zhang et al.'s [18] model, the turbulence dissipation rate is introduced into calculation. The removal rate can be expressed as follows:

$$R_j^{wall} = -\frac{0.0062\varepsilon^{\frac{3}{4}}}{v^{\frac{5}{4}}} \frac{A_s}{V_{cell}} r_j^2 n(V_j, t) \rho_i V_{i,j} \tag{18}$$

where $n(V_j, t)$ represents the current time size j inclusion number density, and the unit for this is n/m^3. A_s and V_{cell} represent local slag cell effective area and volume. ρ_i is the density of inclusion. $V_{i,j}$ is the volume of inclusion with size j.

The second part of the inclusion removal calculation is inclusion removal due to slag absorption. In the current model, when inclusion reaches the slag-steel interface under the influence of the flow field, it is assumed ideally removed by slag. However, when inclusions reach the liquid-free surface in the slag eye zone, they will not be removed, and instead, they will continue to circulate within the steel melt. The removal rate due to slag absorption can be described as:

$$R_j^{slag} = -n(V_j, t)\rho_i V_{i,j} \tag{19}$$

For inclusions attached to bubbles, when the rupture of the bubble occurs at the slag-steel interface, any inclusions attached to the bubble will be considered totally removed. However, similarly to inclusions floating in the melt, when a bubble ruptures at the slag eye zone, any inclusions attached to that bubble will be considered re-released back to steel. The inclusion removal due to bubble attachment can be described as:

$$R_j^{bubble} = -Pu_{rel}\pi\left(r_b^2 + r_{i,j}^2\right)\frac{6\alpha_b}{\pi d_b^3} n(V_j, t)\rho_i V_{i,j} \tag{20}$$

$$P = P_C P_A \tag{21}$$

where u_{rel} is the relative velocity between the gas bubble and inclusion particles; α_b is the volume fraction of gas bubble in the computational cell; P is the efficiency of inclusion

attached to bubble [19]. P consists of two factors: P_C, which represents the probability of inclusion collision with bubbles, and P_A, describing the probability of inclusion attaching to bubbles through adhesion. In this study, based on Trahar's [20] work, the detachment rate of inclusions from bubbles is assumed to be zero. This is an idealized assumption to reduce computational complexity, meaning that when an inclusion attaches to a bubble, it will never detach.

3. Results and Discussion

In this work, the validation ladle model was developed based on published work by Chen et al. [13], and the geometry was used to validate the inclusion aggregation and removal model. The application ladle geometries were developed based on Nucor steel simplified ladle. This geometry was used to simulate and compare the results from flow field and inclusion removal under different operational designs.

3.1. Inclusion Model Validation

As previously mentioned, the geometry used for validation of the inclusion removal model was adopted based on Chen et al.'s work. The upper ladle diameter is 2832 mm, and the lower ladle diameter is 2680 mm. The height of the ladle is 3581 mm. In this work, a flat free-surface was assumed for the top slag-steel interface, and only the liquid steel zone was simulated. A slag eye area was assumed at the upper surface of the steel based on the mathematical model adopted by Krishnapisharody et al., 2008 [21], using the detailed equation listed below:

$$\frac{A_e}{H^2} = -0.76\left(\frac{Q_g}{g^{0.5}H^{2.5}}\right)^{0.4} + 7.15\left(1 - \frac{\rho_s}{\rho_l}\right)^{-0.5}\left(\frac{Q_g}{g^{0.5}H^{2.5}}\right)^{0.73}\left(\frac{h}{H}\right)^{-0.5} \quad (22)$$

where A_e represents slag eye area; H and h are the ladle height and slag thickness, respectively; Q_g is the gas flow rate in m^3/s; ρ_s and ρ_l are slag density and liquid steel density, respectively. The slag thickness, density, argon flow rate, and bubble size utilized are not directly listed in this work but are referred from Chen et al. [13].

The simulation was conducted of this ladle using the proposed inclusion model under operating conditions matching industrial measurements from Miki et al. [22] and an alternative CFD approach by Chen et al. [13]. Figure 1 shows a comparison of inclusion number density distribution at 15 min after the alloys have been added. It can be found from this comparison that the calculated results using the proposed inclusion model are similar to both industrial measurements and Chen et al.'s CFD simulation results. It is also worth noting that both CFD simulation techniques show more deviation in smaller-sized inclusions. It is expected that this occurs because the CFD simulation results neglect rapid re-oxidation and solidification of inclusions during the sampling process, which would be observed in the industrial measurements from Miki et al.

3.2. Model Application: Bottom Injection Refining Ladle

After validation studies, the inclusion removal model was applied to simulate scenarios based on a simplification of a real-world Nucor Decatur ladle. In this design, there are two porous plugs located at the bottom of the ladle for gas injection. Two different variations were simulated for this ladle, one with a plug separation angle of 180°, the other with a plug separation angle of 90°. These two geometries are detailed in Figures 2 and 3.
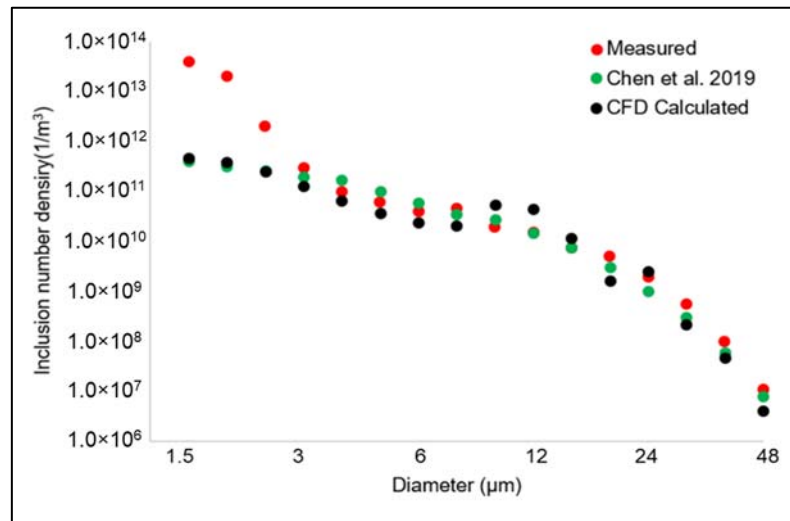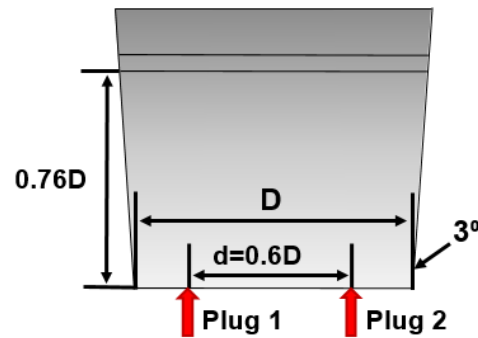
Figure 1. The inclusion number density comparison.

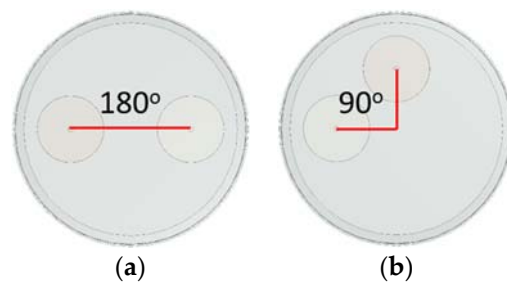
Figure 2. Separation angle of 180° ladle simplified geometry.

Figure 3. Ladle schematic figure: (**a**) plug separation angle of 180°; (**b**) plug separation angle of 90°.

Four scenarios as shown in Table 1 based on operation at the industrial plant were simulated to compare the inclusion removal rate. For bubble size, this study takes the average bubble diameter as the simulation bubble diameter, with the average bubble diameter estimated at 25% of the maximum bubble diameter. Johansen et al. [23] proposed an equation to calculate maximum bubble diameter, expressed as:

$$d_{b,max} = 0.35 \left(\frac{Q_g^2}{g} \right)^{0.2} \tag{23}$$

Table 1. The application ladle condition.

Case No.	Plug Separation Angle	Gas Flow Rate
Case 1	180°	5 and 5 SCFM
Case 2	90°	5 and 5 SCFM
Case 3	90°	5 and 20 SCFM
Case 4	90°	20 and 20 SCFM

3.3. Inclusion Removal Simulation Procedures and Secondary Validation for Application Ladle Flow Field

The distribution of the flow field within the ladle has a significant influence on inclusion removal. Before the inclusion aggregation and removal model is applied, flow field validation of the application ladle geometry is performed by comparing slag eye diameter between CFD results and industrial measurement. A flow rate of 30 SCFM was used for flow field validation.

At the Nucor Decatur steel plant, five measurements of slag eye diameter at a flow rate of 30 SCFM were conducted, indicating a slag eye size between 0.7–0.79 m. In comparison, the slag eye diameters observed in the CFD simulation based on the Euler–Euler multiphase and Euler–Lagrange models are 0.8 m and 0.79 m, respectively. The average error between industrial measurements and CFD results is about 8.8%. Figure 4 shows slag eye size comparison of Euler-Euler multiphase model and Euler–Lagrange multiphase model. It can be found that, as for slag shape and slag eye size, both models produce similar predictions of flow patterns and slag eye size.
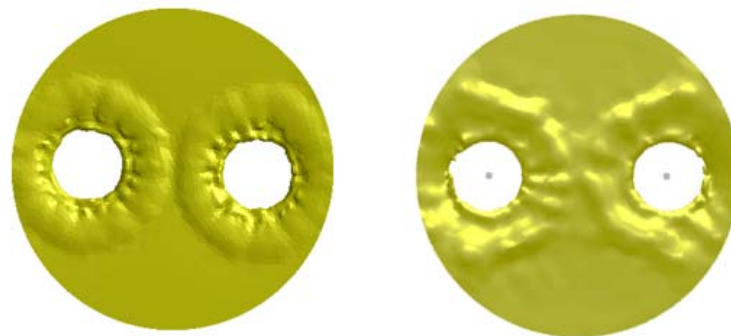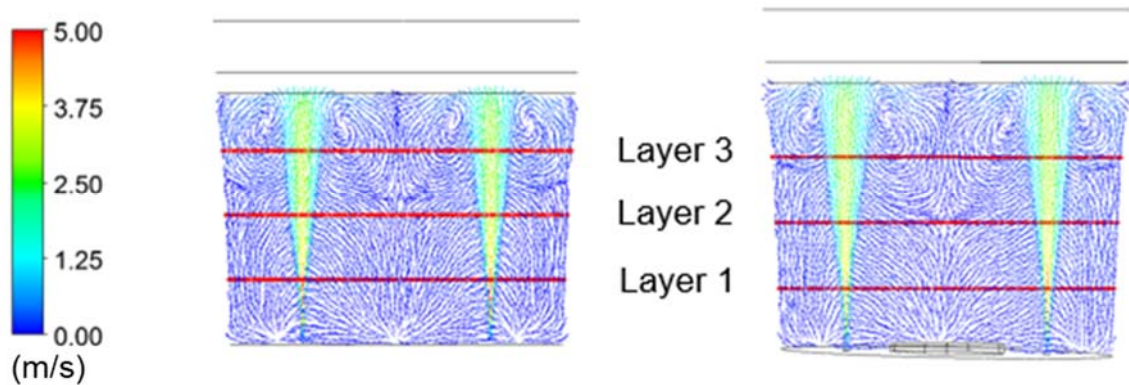

Figure 4. Slag eye size comparison of Euler–Euler multiphase model (**left**) and Euler–Lagrange multiphase model (**right**).

To compare the flow inside of the ladle, three different layers in the ladle are selected to show comparisons between the two models. Figure 5 shows the cross-sectional plane of two ladles. Three monitor layers are also shown in the figure. Figure 6 shows a comparison of velocity at the centerline of the layer. In the simulations presented here, it appears that the fluid velocities observed in the two ladles are very similar. The position where the maximum velocity appears is different, possibly due to the slight change in the geometry.

The shape of the slag eyes and flow fields within the ladles calculated by both the Euler–Euler model and Euler–Lagrange models are very similar. However, it can be difficult to obtain convergence using the Euler–Euler model with three phases, as the model is very sensitive to initial conditions. As for inclusion removal, the shape of slag and slag eye size is important to the overall inclusion removal rate. One solution to this is to utilize the Euler–Lagrange model to first obtain the shape of slag, then run a secondary simulation calculation of the steel computational domain using the Euler–Euler model. This secondary simulation utilizes a top slag-steel interface and interpolates parameters of velocity and turbulence from the calculated slag layer to the Euler–Euler model. After quasi-steady-state hydrodynamics between the molten steel and argon are obtained in the Euler–Euler model,

the population balance model can then be activated to simulated inclusion aggregation and removal.


Figure 5. Flow field comparison and location of three layers.
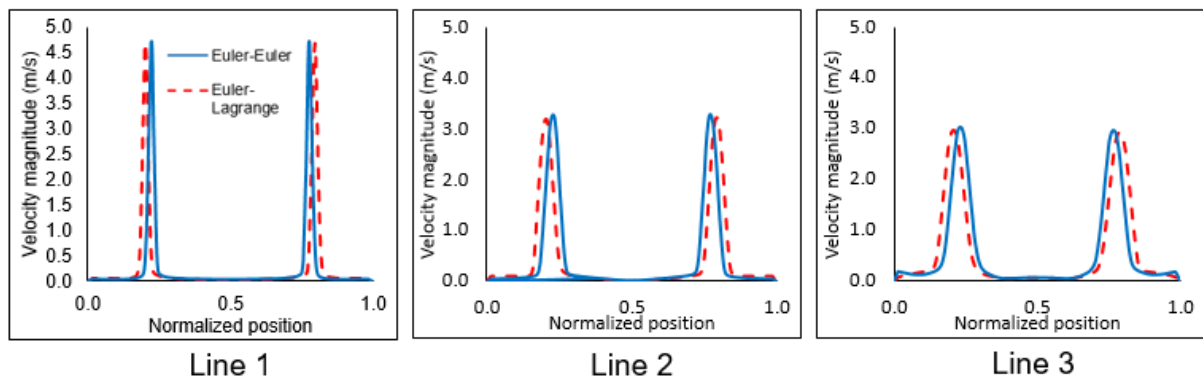
Figure 6. Velocity comparison of the Euler–Euler model and Euler–Lagrange model in centerline.

### 3.4. Impacts of Porous Plug Position on Slag Eye Size and Flow Field

Due to the different plug positions in the two ladle designs, different sets of cross-sectional planes have been created for the 180° and 90° ladles, respectively. As shown in Figure 7, planes 1 and 2 pass through the plugs perpendicularly to the bottom of the ladle, while planes 3 and 4 are located at the center of the ladle and cross planes 1 and 2 at a 90° angle.
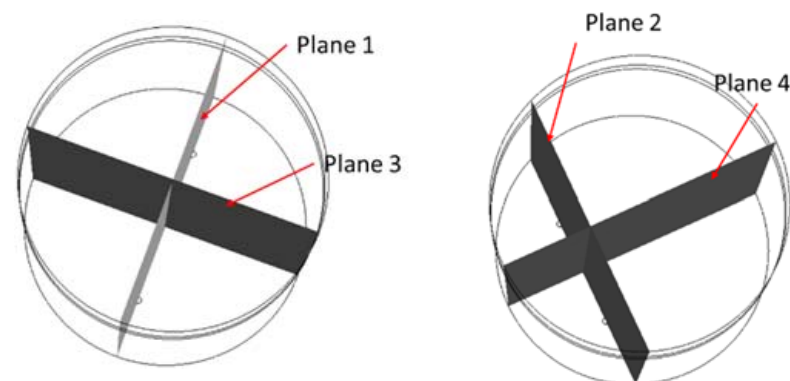
Figure 7. Cross-sectional plane for two ladle geometries: Separation angle of 180° ladle (**left**) and separation angle of 90° ladle (**right**).

Velocity vectors of the steel melt in the ladle set on these cross-sectional planes are shown in Figures 8 and 9. The highest velocity appears in the gas plume region because

the flow there is being accelerated and influenced by the injected gas bubbles. As shown in planes 1 and 2, around the two plume regions, circulations are formed. However, there is some difference between planes 3 and 4. For the 180° ladle, there are two circulations that meet at the center of the plane. For the 90° ladle, these two circulations meet at the center of two plumes. In general, there is always a tendency for molten steel to move to the center of the two gas plumes, and the dead zones wherein the lowest flow velocities and mixing are observed can always be found at the corners of the ladle.
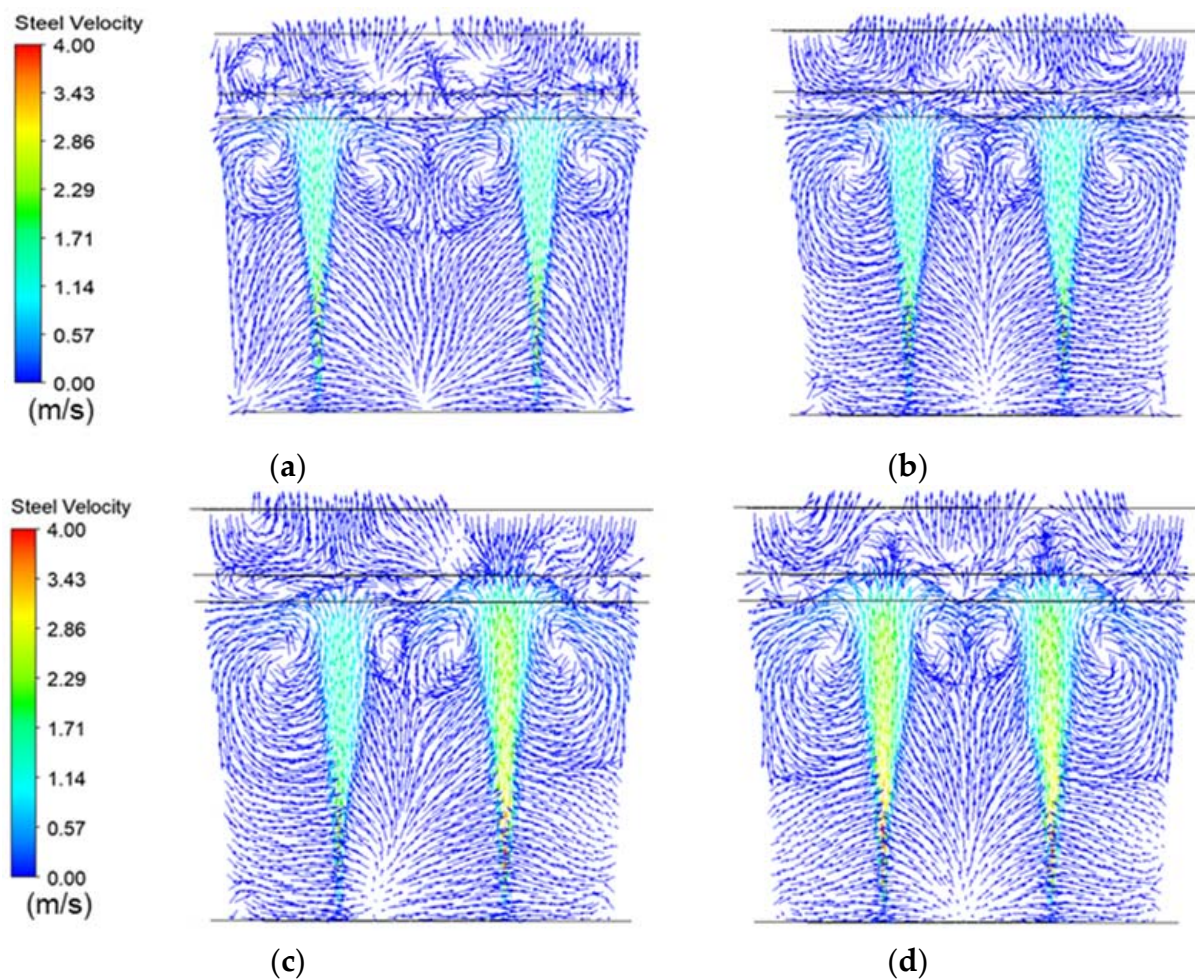

Figure 8. Flow velocity vector in plug cross-section plane: (**a**) 180° 5/5 SCFM, plane 1; (**b**) 90° 5/5 SCFM, plane 2; (**c**) 90° 5/20 SCFM, plane 2; (**d**) 90° 20/20 SCFM, plane 2.

Slag eye size is a critical factor in controlling steel cleanliness during the steel-refining process in the ladle. Normally, slag eye size has a positive correlation with the gas flow rate, but in some cases, the ladle geometry can also affect the size of the slag eye. In this study, the slag eye size has been measured for the 180° and 90° porous plug location designs under different argon gas flow rates. As shown in Figure 10, under an argon flow rate of 5 SCFM for both plugs, whether at 180° or 90°, there is no slag eye generated. When the plug separation angle is fixed, increasing the argon gas flow rate, the slag eye size will increase.

Table 2 shows the mean diameter of slag eye for all different cases. In the scenarios tested, the CFD simulations also indicated that using two plugs with different flow rates can result in a slightly larger slag eye size for one of the plugs, though a smaller total area of liquid steel exposed to the atmosphere compared to using two high gas injection rates.
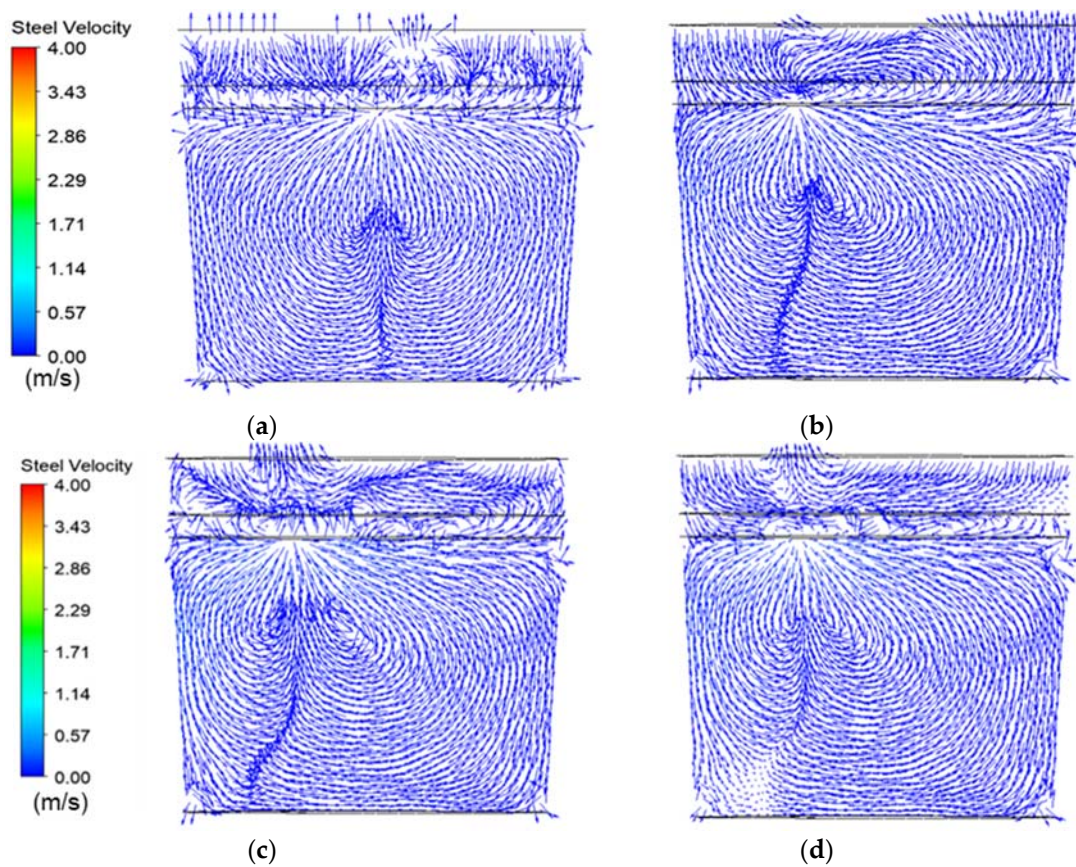
Figure 9. Flow velocity vector in center plane: (**a**) 180° 5/5 SCFM, plane 3; (**b**) 90° 5/5 SCFM, plane 4; (**c**) 90° 5/20 SCFM, plane 4; (**d**) 90° 20/20 SCFM, plane 4.
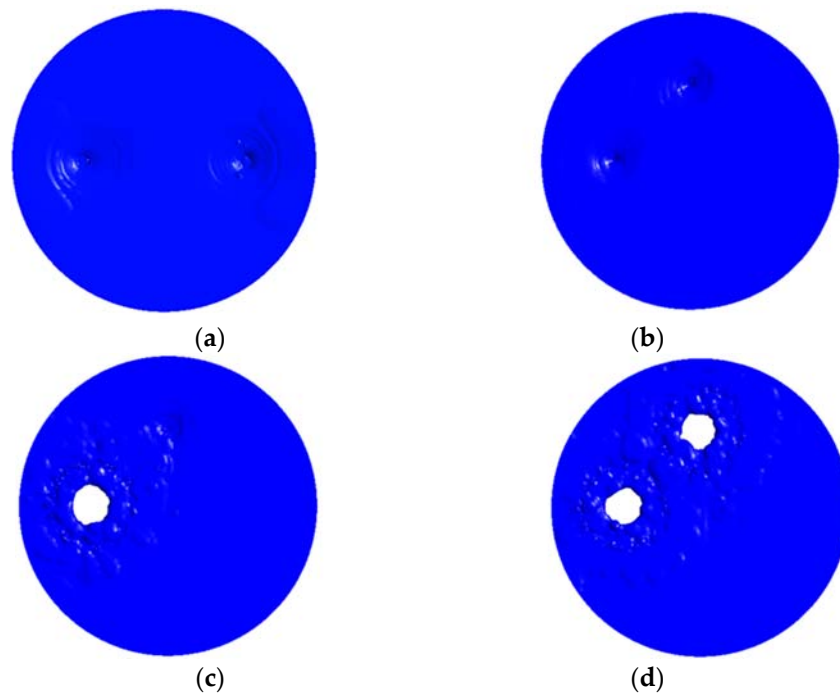
Figure 10. Slag eye size and shape for different cases: (**a**) 180° 5/5 SCFM; (**b**) 90° 5/5 SCFM; (**c**) 90° 5/20 SCFM; (**d**) 90° 20/20 SCFM.

Table 2. The mean diameter of slag eye for different cases.

Case	Slag Eye Diameter (m)
Case 1 (180° 5/5 SCFM)	0
Case 2 (90° 5/5 SCFM)	0
Case 3 (90° 5/20 SCFM)	0.64
Case 4 (90° 20/20 SCFM)	0.62

3.5. Inclusion Behavior Analysis–Aggregation and Removal

3.5.1. Effect of Inclusion Aggregation Mechanism

The inclusion aggregation rate is the summation of two different mechanisms: inclusion aggregate due to turbulent collision and inclusion aggregation due to stokes collision. In order to find out which mechanism is dominant during the inclusion aggregation process, several scenarios were examined without considering inclusion removal mechanisms. Figure 11 shows a comparison of the inclusion number density distribution due to different aggregation mechanisms at 600 s, in the 180° ladle geometry, 5/5 SCFM (case 1). It is immediately apparent that the more aggregation mechanisms are considered in the simulation, the higher the aggregation rate will be. Stoke collision is more important than turbulence in the prediction of the aggregation of larger particles, while turbulence collision is more dominant in the prediction of the aggregation of smaller particles.
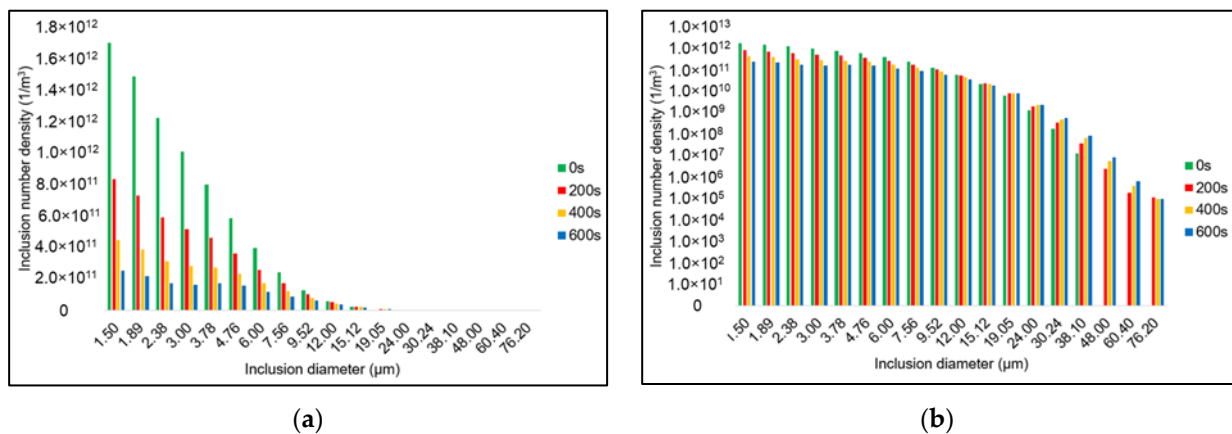

(**a**)   (**b**)
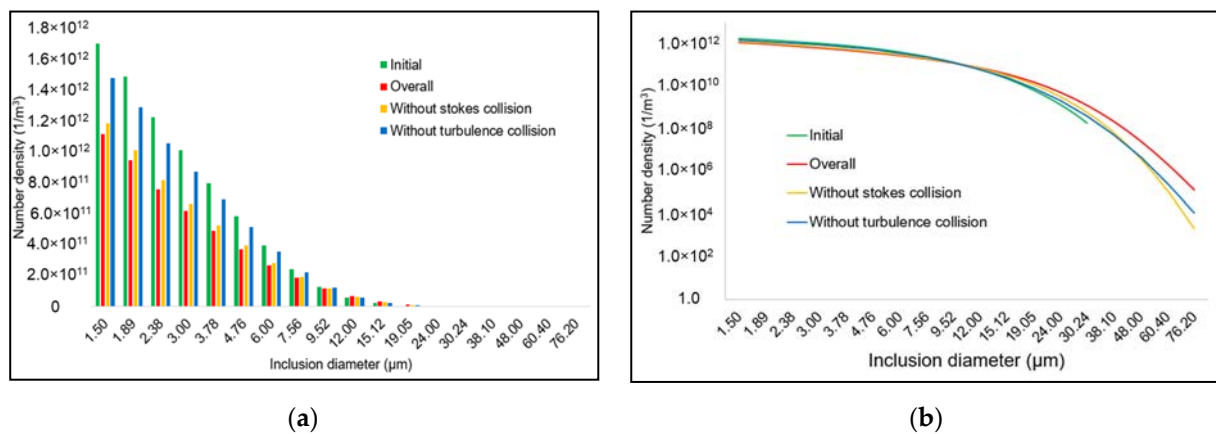
Figure 11. A comparison of inclusion number density distribution due to different aggregation mechanisms at 600 s in case 1: (**a**) number density un-normalized; (**b**) number density normalized.

3.5.2. Effect of Inclusion Aggregation and Removal

As mentioned previously, inclusion removal includes three different mechanisms. They are inclusion removal due to wall adhesion, slag absorption, bubble attachment. In reality, the bubble is only the carrier that transports the inclusion to the slag or walls. After the bubble breakup, inclusion will be eventually removed by slag or wall. However, in order to find out how much inclusion will be carried by bubbles, the bubble removal mechanisms must be defined. In this study, inclusion removal mechanism contribution will be examined using different ladle designs and flow rates.

Figure 12 shows how the inclusion number density in the 180° ladle changes with time. It can be seen that there is no diameter of inclusion greater than 38.1 micrometers distributed in the ladle at the very beginning of the simulation. As flow continues, larger-sized inclusions will appear, and their number density will increase. As for smaller size inclusion, their number density continues to decrease as time passes. From the beginning to the end of the simulation, the ladle was mainly occupied by inclusions of smaller size.

(**a**)　　　　　　　　　　　　　　　　　　　(**b**)

Figure 12. Inclusion number density distribution at different flow times, in case 1: (**a**) number density un-normalized; (**b**) number density normalized.

As shown in Figure 13, the mass of inclusions in all four cases decreases steadily over time. The overall removal rates for cases 1 through 4, respectively, are 45.2%, 43.9%, 51.7%, and 56.4%. It is also worth noting here that both case 3 (90° 5/20) and case 4 (90° 20/20) have at least one slag eye. In the current model, re-oxidation is not considered, so the overall removal rate of these two cases can be overestimated. The removal rates observed in the simulations for case 1 (180° 5/5) are higher than in case 2 (90° 5/5). A larger plug separation angle promotes the inclusion removal rate.
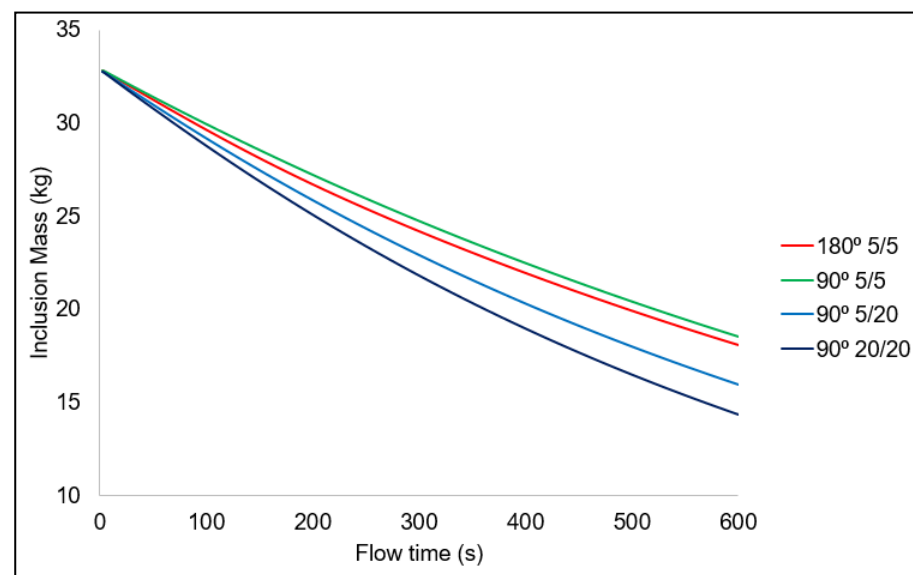
Figure 13. The mass of inclusion change over time in four cases.

Figure 14 shows a comparison of the inclusion removal rate due to different mechanisms over time for the four different scenarios. It can be found that slag abortion is dominating the inclusion removal rate in four scenarios, while wall adhesion contributes the least removal rate. For the inclusion removal rate due to bubble attachment, any inclusions attached to bubbles are considered. Whether the inclusion is then eventually removed at the slag-steel interface or re-released at the slag eye area is not included in this comparison. In general, as the gas flow rates increase, without considering re-oxidation from slag eye, the inclusion removal rate will increase.

(**a**)

(**b**)

(**c**)
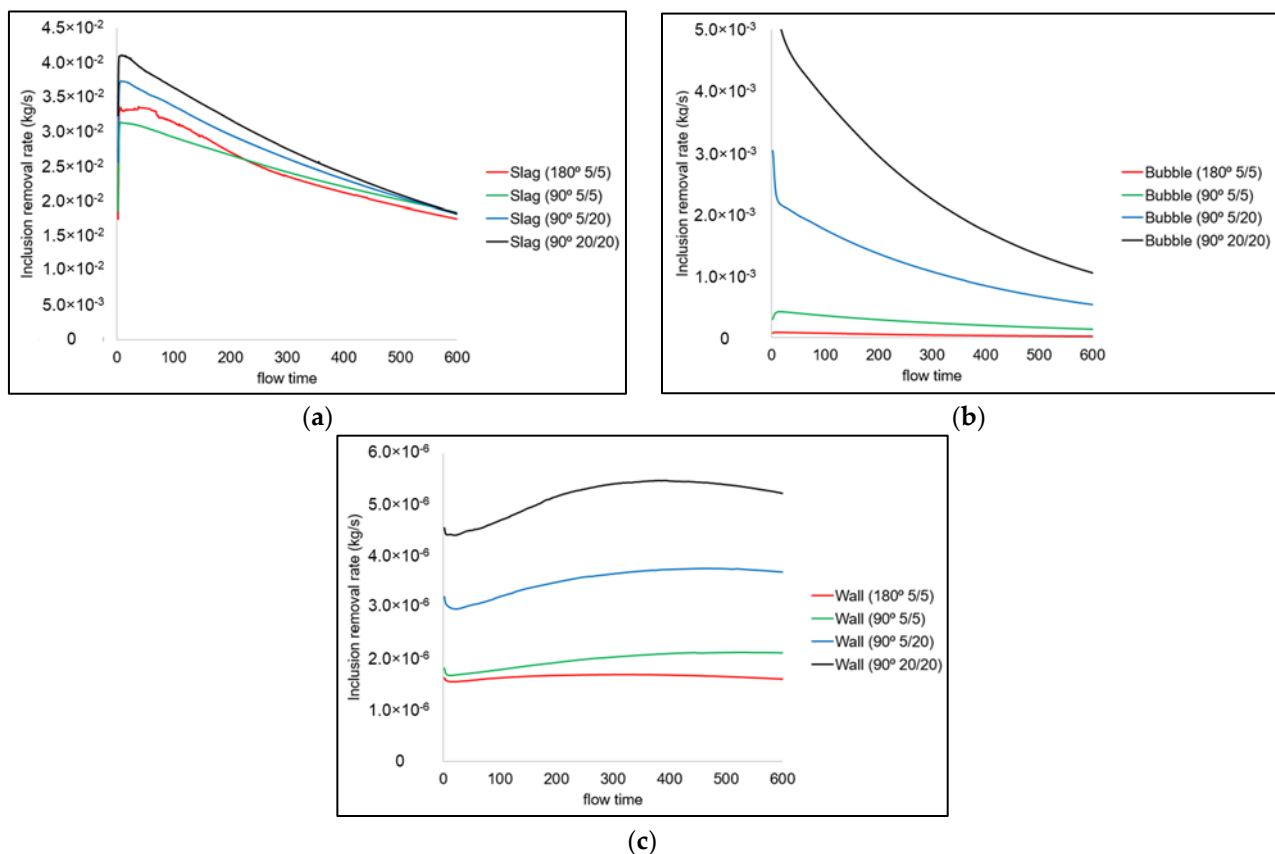
Figure 14. A comparison of the inclusion removal rate due to three mechanisms in different ladles: (**a**) slag absorption; (**b**) bubble attachment; (**c**) wall adhesion.

4. Conclusions

An unsteady, three-dimensional, isothermal, multiphase computational fluid dynamics (CFD) model was developed for simulating fluid flow and inclusion agglomeration and removal in a steel-refining ladle. The inclusion aggregation and removal model is validated by comparing simulated inclusion number density distribution with experimental measurements. With this model, a comprehensive study of inclusion aggregation and removal in different bottom gas-stirred ladles was conducted. Based on a simplified Nucor Steel two-plug bottom injection ladle, two different separation angle ladle cases, 180° and 90°, were developed. Three argon gas flow rate combinations (5/5 SCFM, 5/20 SCFM, and 20/20 SCFM) were employed across these ladle designs. Inclusion aggregation and removal in different ladles have been investigated.

A study of the impacts of ladle design and flow rate on inclusion aggregation and removal has been conducted utilizing the aforementioned CFD model. Key findings include notes on the impacts of gas flow rates on slag eye formation and the further impacts of these conditions on inclusion aggregation and removal. Without considering re-oxidation at slag eye, for a fixed gas flow rate, an increase in plug separation angle will result in an increase in the inclusion removal rate. This was demonstrated by comparing 180° and 90° separation angles. Likewise, when the plug separation angle is fixed, and the gas flow rate increases, the inclusion removal rate will also increase.

Further research may be necessary to explore the potential impacts of these design modifications. A comparison of potential erosion on the ladle wall due to shear stress may be necessary to ascertain whether the increased flow rate near the ladle walls would result in shorter lifespans for refining ladles, and correspondingly whether adjusting the position of porous plugs would present a beneficial design modification for industrial facilities.

References

1. Szekely, J.; Asai, S. The general mathematical statement of turbulent recirculatory flows. *Trans. Iron Steel Inst. Jpn.* **1975**, *15*, 270–275. [CrossRef]
2. DebRoy, T.; Majumdar, A.K.; Spalding, D.B. Numerical prediction of recirculation flows with free convection encountered in gas-agitated reactors. *Appl. Math. Model.* **1978**, *2*, 146. [CrossRef]
3. Johansen, S.T.; Robertson, D.G.C.; Woje, K.; Engh, T. Fluid dynamics in bubble stirred ladles: Part I. Experiments. *Metall. Mater. Trans. B* **1988**, *19*, 745–754. [CrossRef]
4. Peranandhanthan, M.; Mazumdar, D. Modeling of slag eye area in argon stirred ladles. *ISIJ Int.* **2010**, *50*, 1622–1631. [CrossRef]
5. Mazumdar, D.; Guthrie, R.I.L. Modeling energy dissipation in slag-covered steel baths in steelmaking ladles. *Metall. Mater. Trans. B* **2010**, *41*, 976–989. [CrossRef]
6. Guo, D.; Irons, G.A. Modeling of gas-liquid reactions in ladle metallurgy: Part II. Numerical simulation. *Metall. Mater. Trans. B* **2000**, *31*, 1457–1464. [CrossRef]
7. Zhang, L. Mathematical simulation of fluid flow in gas-stirred liquid systems. *Modell. Simul. Mater. Sci. Eng.* **2000**, *8*, 463. [CrossRef]
8. Lou, W.; Zhu, M. Numerical simulation of gas and liquid two-phase flow in gas-stirred systems based on Euler-Euler approach. *Metall. Mater. Trans. B* **2013**, *44*, 1251–1263. [CrossRef]
9. Lou, W.; Zhu, M. Numerical simulations of inclusion behavior in gas-stirred ladles. *Metall. Mater. Trans. B* **2013**, *44*, 762–782. [CrossRef]
10. Shirabe, K.; Szekely, J. A mathematical model fluid flow inclusion coalescence RH vacuum degassing system. *ISIJ Int.* **1983**, *23*, 465. [CrossRef]
11. Söder, M.; Jönsson, P.; Jonsson, L. Inclusion growth and removal in gas-stirred ladles. *Steel Res. Int.* **2004**, *75*, 128–138. [CrossRef]
12. Wang, L.T.; Peng, S.H.; Zhang, Q.Y.; Li, Z.B. Mathematical model for growth and removal of inclusions in molten steel under gas-stirring conditions. *Steel Res. Int.* **2006**, *77*, 25–31. [CrossRef]
13. Chen, G.; He, S. Application of inhomogeneous discrete method to the simulation of transport, agglomeration, and removal of oxide inclusions in a gas-stirred ladle. *JOM* **2019**, *71*, 4206–4214. [CrossRef]
14. Miyashita, Y.; Nishikawa, K. Corrigenda to "Measurement of the Size Distribution of Nonmetallic Inclusions in Steel". *Trans. Iron Steel Inst. Jpn.* **1968**, *8*, 181–185. [CrossRef]
15. Yue, Q.; Chen, H.-H.; Jia, X.-F.; Kong, H. Kinetic study on collision and aggregation of non-metallic inclusion in liquid steel. *Metal. Int.* **2014**, *22*, 19.
16. Saffman, P.G.F.; Turner, J.S. On the collision of drops in turbulent clouds. *J. Fluid Mech.* **1956**, *1*, 16–30. [CrossRef]
17. Abrahamson, J. Collision rates of small particles in a vigorously turbulent fluid. *Chem. Eng. Sci.* **1975**, *30*, 1371–1379. [CrossRef]
18. Zhang, L.S.; Taniguchi, S.; Cai, K. Fluid flow and inclusion removal in continuous casting tundish. *Metall. Mater. Trans. B* **2000**, *31*, 253–266. [CrossRef]
19. Wang, L.; Lee, H.-G.; Hayes, P. Prediction of the optimum bubble size for inclusion removal from molten steel by flotation. *ISIJ Int.* **1996**, *36*, 7–16. [CrossRef]
20. Trahar, W.J. A rational interpretation of the role of particle size in flotation. *Int. J. Miner. Process.* **1981**, *8*, 289–327. [CrossRef]
21. Krishnapisharody, K.; Irons, G.A. An extended model for slag eye size in ladle metallurgy. *ISIJ Int.* **2008**, *48*, 1807–1809. [CrossRef]
22. Miki, Y.; Thomas, B.G. Modeling of inclusion removal in a tundish. *Metall. Mater. Trans. B* **1999**, *30*, 639–654. [CrossRef]
23. Johansen, S.T.; Boysan, F. Fluid dynamics in bubble stirred ladles: Part II. Mathematical modeling. *Metall. Trans. B* **1988**, *19*, 755–764. [CrossRef]